J. Plasma Physics (2012), vol. 78, part 4, pp. 355–361. © Cambridge University Press 2012
doi:10.1017/S0022377812000062

Straight and linearly tapered capillaries produced by femtosecond laser micromachining

S. M. WIGGINS[1], M. P. REIJNDERS[1,2], S. ABUAZOUM[1], K. HART[1], G. VIEUX[1], G. H. WELSH[1], R. C. ISSAC[1], X. YANG[1], D. R. JONES[1] and D. A. JAROSZYNSKI[1]

[1]Scottish Universities Physics Alliance, Department of Physics, University of Strathclyde, Glasgow G4 0NG, UK (mark.wiggins@strath.ac.uk)
[2]TMC Physics, Flight Forum 107, 5657 DC Eindhoven, The Netherlands

(Received 28 September 2011; revised 14 November 2011; accepted 5 January 2012; first published online 2 February 2012)

Abstract. Gas-filled capillary discharge waveguides are a commonly employed medium in laser–plasma interaction applications, such as the laser wakefield accelerator, because they can simultaneously guide high-power laser pulses while acting as the medium for acceleration. In this paper, the production of both straight and linearly tapered capillaries using a femtosecond laser micromachining technique is presented. A tapered capillary is shown to possess a smooth variation in diameter (from 305 μm to 183 μm) along its entire 40 mm length, which would lead to a longitudinal plasma density gradient, thereby dramatically improving the laser–plasma interaction efficiency in applications. Efficient guiding with up to 82% energy transmission of the fundamental Gaussian mode of a low intensity, 50 fs duration laser pulse is shown for both types of capillary waveguide.

1. Introduction

The gas-filled capillary discharge waveguide (CDW) is a useful medium for high-power laser–plasma interactions because the efficient guiding process increases the interaction length up to several 10 s of Rayleigh lengths [1]. Two important applications are the laser-wakefield accelerator (LWFA) [2, 3], for generation of ultra-short electron beams of GeV-scale energies [4] and bright gamma-ray radiation pulses [5], and the chirped pulse Raman amplifier (CPRA) [6, 7] for resonant energy transfer from a long pump pulse to an ultra-short probe pulse [8]. The former shows huge potential as a compact driver for next-generation light sources [9] and particle accelerators [10] while the latter aspires to provide an alternative amplifying medium to chirped pulse amplification [11] and optical parametric chirped pulse amplification [12] schemes for future large-scale laser systems [13].

Plasma is formed in a gas-filled CDW before the arrival of the laser pulse(s) by injection of gas (usually hydrogen) and subsequent ionization by a ~20 kV sub-microsecond electrical discharge pulse [14]. The high laser intensities and high voltages that are applied to the waveguide demand that hard materials such as sapphire or alumina are utilized for maximum robustness. Hence, femtosecond laser micromachining [15] has become a common technique for their production [16] because of its inherent precision, repeatability and determinism [17].

In this paper, we outline one micromachining technique for straight capillaries providing a uniform longitudinal plasma density and extend it to the micromachining of capillaries featuring a linear taper in their diameter. Tapering the diameter, i.e. the cross-section, results in a longitudinal plasma density gradient [18] that may benefit both the LWFA by increasing the final electron beam energy [19–21] and the CPRA by increasing the seed laser amplification efficiency [6]. In Sec. 2, the micromachining experimental setup is presented in the context of producing straight capillaries. The micromachining methodology is extended to linearly tapered waveguides in Sec. 3. Results characterising the plasma and showing efficient guiding of low intensity, femtosecond duration laser pulses are presented for both capillary types in Sec. 4 and, finally, a conclusion and discussion are given in Sec. 5.

2. Machining straight capillaries

The schematic composition of our gas-filled CDW system is shown in Fig. 1. To produce a waveguide, identical channels or grooves with a semi-circular cross-section are machined into two plates of a hard insulating material, typically sapphire or alumina. When the plates are carefully aligned and glued together, a high aspect ratio circular cross-section channel is formed, which acts as a robust capillary for containing the plasma. Machining is achieved by scanning a focused, high repetition rate, femtosecond laser over the plates' surface. Additional holes or grooves are machined to form gas injection channels. Copper electrodes, coupled to the output of a high voltage pulsed power supply, are positioned at either end of the capillary. On-axis apertures enable the laser pulses to propagate. Plasma is generated upon

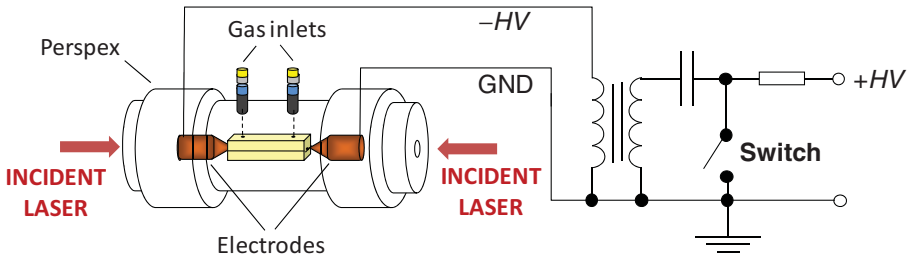

Figure 1. (Colour online) Schematic composition of the gas-filled capillary discharge waveguide setup. Pulsed power supply details are given in [22].

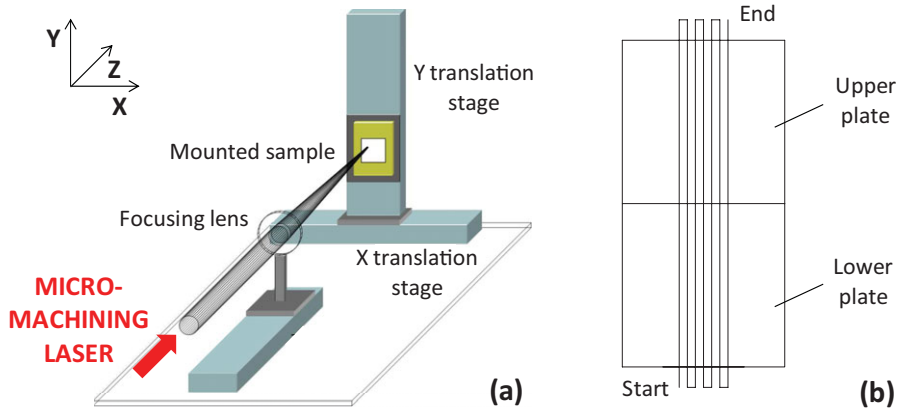

Figure 2. (Colour online) (a) Experimental setup used to perform femtosecond laser micromachining and (b) schematic representation of the scanning laser path for machining a straight CDW.

applying a potential difference of ∼20 kV across the capillary (typically 30–40 mm in length) and subsequent rapid avalanche breakdown [22]. Formation of a high current (∼300 A) discharge pulse is evidence of near complete ionization of the gas in the capillary [14].

The experimental setup to perform femtosecond laser micromachining is shown in Fig. 2(a). Machining is conducted using the Strathclyde Terahertz to Optical Pulse Source (TOPS) femtosecond laser system [23] (intensity $\approx 10^{14}$ W/cm^2, duration = 50 fs, focal spot radius at $1/e^2$ of $w_0 = 12\,\mu$m and 1 kHz pulse repetition rate). The focusing lens is mounted on a Z translation stage for precise location of the focal position at the surface plane of the plates that are mounted together on XY translation stages. All stages are driven by a computer-controlled motion controller (Newport, XPS) such that position and velocity commands sent to the controller determine the pattern to be machined.

There are two key aspects of the femtosecond laser micromachining process that influence the scheme for obtaining a circular cross-section. Firstly, the laser focal spot size is much less than the capillary diameter. Secondly, as a laser beam scans across the target surface, the cross-sectional area of ablated material is inversely proportional to the scanning velocity (see Appendix A). The individual pulses overlap, therefore, for the relevant velocity range and the laser can be assumed to be continuous. A circular cross-section requires the greatest amount of laser ablation to take place on-axis with progressively less occurring towards the edges and this is achieved with a near-hemispherical scanning velocity profile mapped onto a hemispherical machined depth profile (slowest scan velocities on-axis and fastest at the outer edges). A complete capillary is machined with a series of *longitudinal (Y)* scan lines at different *radial (X)* positions. The schematic of Fig. 2(b) depicts such seven scan lines; in fact, 57 scan lines are applied and the entire "loop" is repeated 16 times.

The basis, therefore, for machining a uniform, straight capillary is constant velocity motion of the scanning laser along the longitudinal direction utilizing this velocity-to-depth mapping. The capillary diameter d is set by the radial step size δx between longitudinal scans with matched laser energy to achieve the corresponding depth profile ($d/2$ in the center). The optimal, matched energy setting results in the desired semi-circular depth profile, otherwise grooves are too deep or too shallow, as shown in Fig. 3. The machined depth scales linearly with average laser pulse energy and energy fluctuations during the long machining times (95 min in the case of a 40 mm long straight capillary) are the primary cause of any ellipticity in the final capillary cross-section. If the average laser energy (monitored with a photodiode) drifts outside an acceptable range (typically set at $\pm 10\%$), the control program (National Instruments, LabVIEW [24]) pauses the machining process to allow correction.

A photograph of a completed CDW is displayed in Fig. 4(a) and optical microscope images of an example straight capillary are shown in Fig. 4(b). The latter

https://doi.org/10.1017/S0022377812000062 Published online by Cambridge University Press

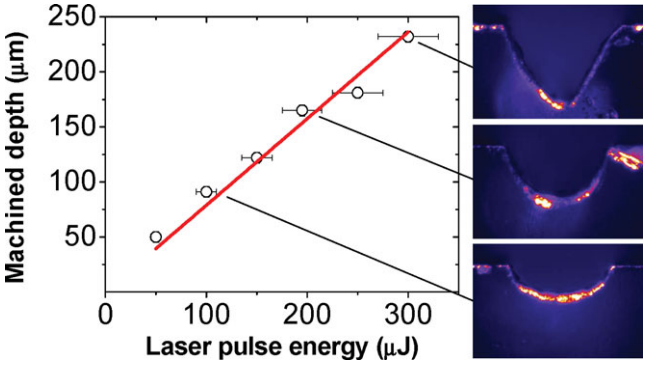

Figure 3. (Colour online) Machined depth as a function of scanning laser pulse energy (with ±10% fluctuations) and three corresponding false colour optical microscope images of groove cross-sections that are too deep, near optimal and too shallow, respectively, from top to bottom. The solid line is a best-fit straight line.

alumina capillary is of length 40 mm and nominal design diameter 280 μm. The laser pulse energy was 150 μJ (corresponding to intensity 10^{14} W/cm^2). A high degree of circularity to the capillary channel is evident and the measured on-axis machined depth is (303 ± 3) μm. This is 8% larger than the design diameter with laser energy drift accounting for the discrepancy. Note the splayed edges at the extremities of each machined plate [Fig. 4(b)] that are present to eliminate any risk of surface cracking.

3. Machining linearly tapered capillaries

A linear taper in the diameter requires two modifications of the machining process. Firstly, the scanning direction is not wholly longitudinal; a small radial velocity component is also needed along each plate to obtain the conical shape, as shown in the modified scanning schematic of Fig 5(a). Secondly, as the scanning laser progresses from the wide end to the narrow end, its velocity must increase to maintain the semi-circular ablation depth (which is inversely proportional to the velocity). Hence, the scanning laser is now accelerating instead of moving at constant velocity. The tapered capillary trajectory equations describing the evolution of the scanning laser position $x(t)$, velocity $v(t)$ and acceleration $a(t)$ as a function of time t, per scan line, are

$$x(t) = \frac{1}{\alpha}\left(\sqrt[3]{3tr_1^2v(0)\alpha + r_1^3} - r_1\right), \tag{1}$$

$$v(t) = \frac{r_1^2 v(0)}{\left[r_1^2 3tv(0)\alpha + r_1^3\right]^{2/3}}, \tag{2}$$

$$a(t) = \frac{-2r_1^4 v(0)^2\alpha}{-r_1^2\left[-3tv(0)\alpha - r_1\right]^{5/3}}, \tag{3}$$

where $\alpha = (r_2 - r_1)/L$ describes the rate of tapering, r_1 and r_2 are the start and end radii, respectively, L is the

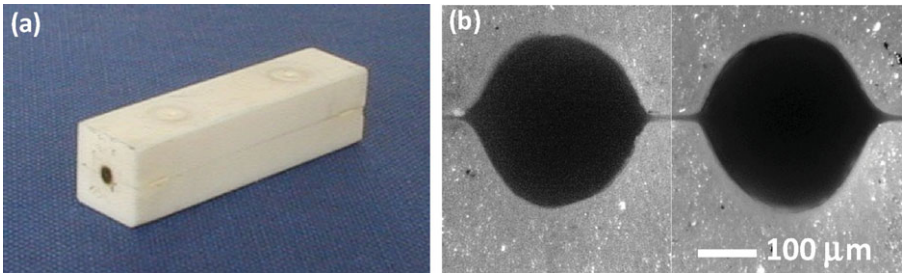

Figure 4. (Colour online) (a) Photograph of a finished, used alumina CDW (length 40 mm). Dark carbonization adjacent to the cathode location is seen around the waveguide entrance and the two gas inlets are visible on the top surface. (b) Optical microscope images of a straight CDW showing both ends of the aligned capillary. The indicated scale applies to both images.

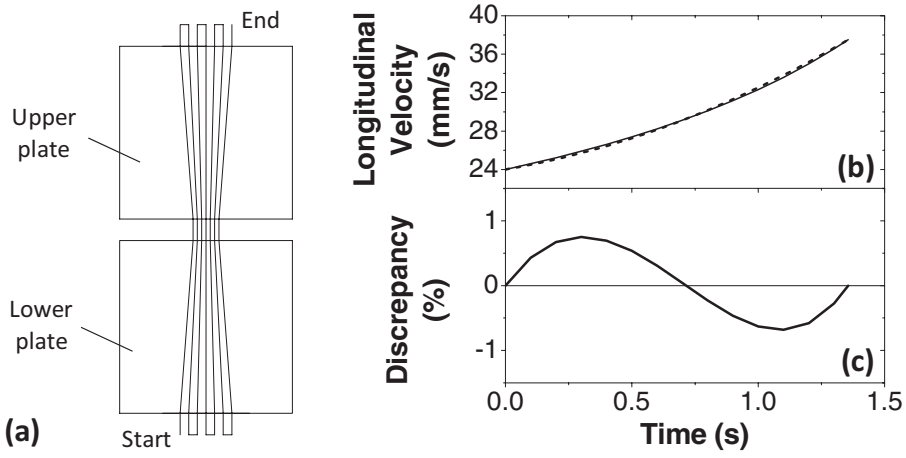

Figure 5. (a) Schematic representation of the scanning laser path for machining a linearly tapered CDW. Note the spacer between the plates in the latter. (b) Longitudinal scanning laser velocity for the outermost scan lines of a tapered capillary of diameter 280 μm to 224 μm and length 40 mm. The solid curve depicts the desired velocity given by (2), the dashed curve depicts the actual velocity implemented by the PVT mode of the motion controller and (c) shows the discrepancy between the two velocities.

https://doi.org/10.1017/S0022377812000062 Published online by Cambridge University Press

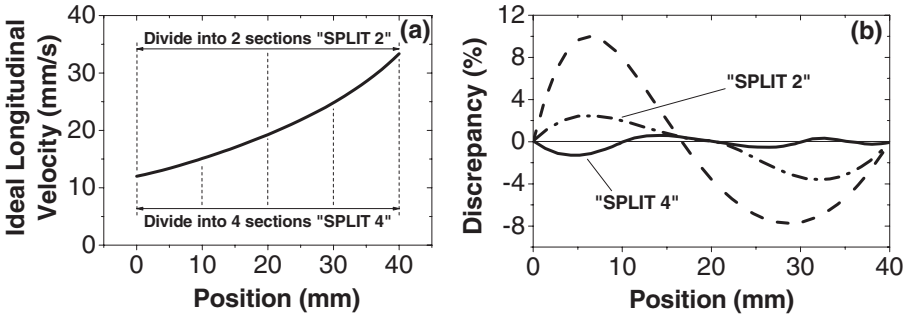

Figure 6. (a) Longitudinal scanning laser velocity for the outermost scan line of a tapered capillary of diameter 280 μm to 168 μm and length 40 mm depicting the "Split 2" and "Split 4" sub-divisions of the scan line. (b) Discrepancy between the ideal velocity and actual PVT velocity for the original (dashed curve), "Split 2" (dash dotted curve) and "Spilt 4" (solid curve) PVT trajectories.

length and $v(0)$ is the initial velocity for that particular scan line (see Appendix B).

The angled accelerating scan lines can be implemented by the XPS motion controller operating in its Position, Velocity, and Time (PVT) trajectory mode. The calculated PVT trajectory, however, is constrained by a linear rate of change of acceleration, i.e. constant jerk, that leads to third- and second-order polynomial expressions for position $x(t)$ and velocity $v(t)$, respectively. Hence, there is a small discrepancy between the ideal velocity evolution given by (2) and the real velocity evolution outcome (likewise for the subsequent CDW plasma density). For weak tapering, the discrepancy is negligible (less than 1%) as shown in the example of Fig. 5(b) for a 40 mm long capillary tapering from 280 μm to 224 μm.

When the tapering is stronger, the discrepancy can become problematic. For example, with a 40 mm long capillary tapering from 280 μm to 168 μm, the magnitude of the discrepancy peaks at 10% and the machined longitudinal depth profile deviates appreciably from the desired profile (the velocity may even fail to increase monotonically with distance). However, in these cases, excellent agreement (discrepancy of 1% or less) between the ideal and actual velocity evolutions can be recovered by splitting the longitudinal scan line up into subsections. As shown in Fig. 6 for the aforementioned taper, splitting into two sections ("Split 2") reduces the mean discrepancy from 5.5% to 1.6% while splitting into four sections ("Split 4") reduces it to only 0.4%. Suffice to say, a more sophisticated motion controller would eliminate the need for this trajectory splitting correction, although, its use may still be required for future exotically structured capillaries, e.g. nonlinear undulations or tapers.

Optical microscope images of an example strongly linearly tapered capillary are shown in Fig. 7. The alumina capillary is of length 40 mm and nominal design diameter is 280 μm $\rightarrow$ 168 μm ($\alpha = 1.4 \times 10^{-3}$ and laser pulse energy is $\sim$150 μJ). No scan line splitting has been implemented in this example. Imaging of the longitudinal capillary widths [Figs. 7(a) and (b)] demonstrate that a smooth taper from the wide end to the narrow end has been accomplished along both plates. The end-on images, after aligning the two plates

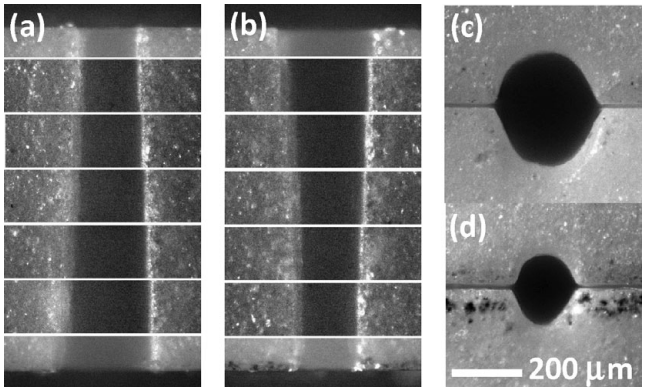

Figure 7. (a) Optical microscopy images of a linearly tapered capillary showing regular longitudinal positions along the (a) lower and (b) upper plate surfaces. (c) and (d) show each end of the aligned capillary. The indicated scale applies to all images.

together, are shown in Figs. 7(c) and (d). Dimensions of the major and minor axes for each best-fit ellipse are 330 $\times$ 280 μm and 196 $\times$ 170 μm, respectively. The aspect ratio of 1.16 $\pm$ 0.02 indicates that the average laser energy increased markedly from the optimal setting during the machining time (106 min in this case) but note that the end-to-end cross-section area reduction factor of 2.77 is equal to that of the nominal design.

4. Plasma properties and femtosecond laser guiding

Straight and linearly tapered CDWs have been characterized with respect to both their plasma and laser guiding properties. The experimental setup is shown in Fig. 8. The femtosecond laser is that used for the micromachining but strongly attenuated to a focal intensity of $\approx 10^{12}$ W/cm^2. The capillary under investigation is mounted in a compact vacuum unit and a hydrogen gas backing pressure $\sim$50 mbar is applied. Near full ionization along the capillary is achieved upon application of a 22 kV, 900 ns voltage pulse from a pulsed power supply based on solid-state switching and transmission-line transformer [22]. The diagnostics comprise two imaging systems. Firstly, a spatially resolved, time-averaged measurement of the plasma density at

https://doi.org/10.1017/S0022377812000062 Published online by Cambridge University Press

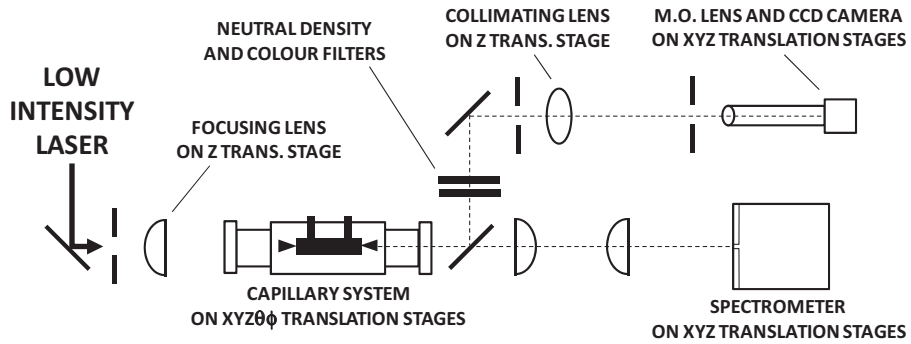

Figure 8. Schematic diagram of the experimental setup for characterizing the plasma and laser guiding of manufactured CDWs. The laser propagation axis is denoted by the ordinate Z and M.O. denotes microscope objective (magnification factor of 4).

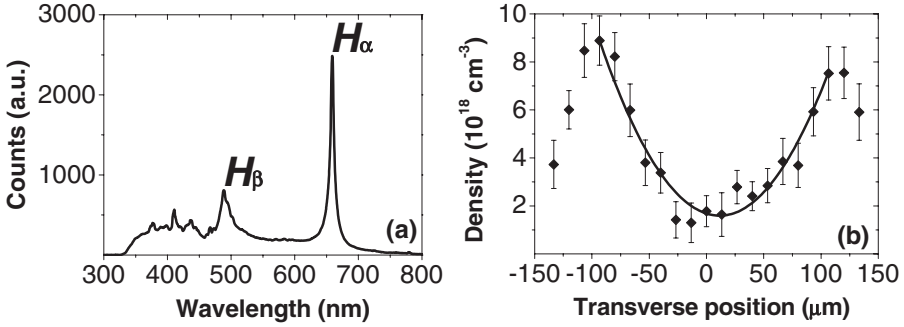

Figure 9. (a) Example hydrogen emission spectrum and (b) transverse (horizontal) time-averaged plasma density profile at one end of a straight CDW of length 40 mm and diameter 286 μm. The zero position denotes the centre of the capillary and the solid curve is a best-fit parabola.

the capillary exit plane can be obtained with an optical spectrometer (5 μm entrance slit and 1.4 nm resolution) that measures the spectra of Stark-broadened Balmer line emission from the background neutral atoms [25]. Secondly, images of the laser spatial profile at both the capillary entrance and exit planes can be obtained with a charge-coupled device (CCD) camera (Point Grey Research, Flea2). The latter allows the laser energy transmission to be determined.

Plasma spectroscopy measurements confirm that the prerequisite under dense plasma with excellent shot-to-shot stability is generated in each CDW. An example captured hydrogen spectrum, showing the Balmer lines H_α (656.27 nm) and H_β (486.13 nm), is presented in Fig. 9(a). The linewidth of the H_α line is used to derive the plasma density while the emission line signal ratio H_α/H_β is used to derive the plasma temperature [25]. Figure 9(b) shows a radial density scan for a straight CDW of length 40 mm and diameter 286 μm. The on-axis, time-averaged plasma density is $(1.7 \pm 0.2) \times 10^{18}$ cm^{-3} and the characteristic parabolic shape of the CDW density is evident with density drop-off close to the walls [18, 26] indicating a channel diameter of $\sim$200 μm. The peak density is expected to be approximately double the time-averaged value and the corresponding time-averaged plasma temperature is $\sim$3–4 eV. However, the measured H_α-derived density is most likely over-estimated by a factor of $\sim$3 when compared with the more accurate transverse interferometry method [27, 28], that is in agreement with a non-local thermal equilibrium (non-LTE) plasma model [29], because of H_α self-absorption and subsequent line broadening in dense plasma [28, 30]. Other measurements confirm the existence of a longitudinal plasma density gradient in the linearly tapered CDWs [31].

Guiding of a low intensity femtosecond laser pulse has been characterized for both types of CDW. Images captured by the CCD camera detection system are shown in Fig. 10. For scale reference, the background plasma emission is displayed in Fig. 10(a). When obtaining quantitative measurements, this signal, which is at shorter wavelengths [Fig. 9(a)] than the laser pulse (central wavelength = 800 nm), is minimized with a colour filter. The laser energy transmission is determined by the ratio of the CCD camera integrated signals at the exit and entrance planes, respectively, both background subtracted and averaged over many shots. Figures 10(a)–(c) show example images captured for a straight capillary. When the laser timing with respect to the current discharge pulse is non-optimal, i.e. too early or too late, the Gaussian shape of the entrance laser is destroyed by the excitation of transverse modes [Fig. 10(c)] and the energy transmission is only (31 ± 3)%. With optimal laser/plasma synchronization, the spatial quality of the laser pulse is preserved [Fig. 10(d)] and the energy transmission is up to (84 ± 7)%. The matched spot size is $\sim$35 μm at the estimated peak density of 3×10^{18} cm^{-3} hence spot size oscillations

https://doi.org/10.1017/S0022377812000062 Published online by Cambridge University Press

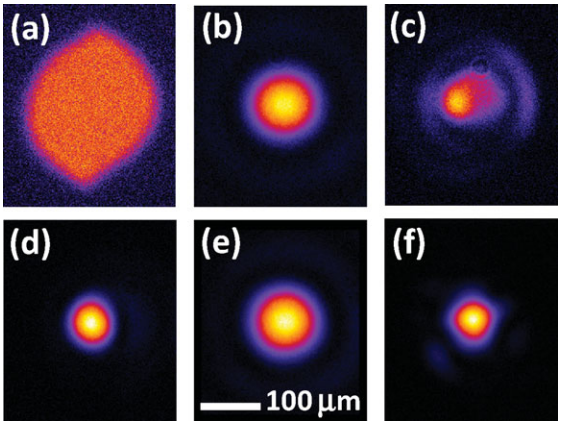

Figure 10. (Colour online) False colour CCD camera images showing (a) background plasma emission, (b) entrance laser pulse, (c) exit laser pulse non-optimally guided and (d) exit laser pulse optimally guided for a straight CDW of length 40 mm and diameter 296 μm. (e) and (f) show the entrance and optimally guided exit laser pulse, respectively, for a tapered CDW of length 40 mm and diameter 320 μm to 270 μm. The indicated scale applies to all images.

(scalloping) occur along the waveguide [1] and the exit beam size is smaller than that at the entrance (w_0 reduces from 81 μm to 47 μm). Similar results are obtained for a linearly tapered CDW as shown in Figs. 10(e) and (f). Here the energy transmission is up to $(82 \pm 9)\%$ so the guiding is seen to be equally efficient for the case of a longitudinally tapered plasma density.

The laser energy loss (~15%–20%) during propagation through the waveguide can be attributed to inverse bremsstrahlung absorption [32] where, at low-laser intensity, the absorption rate is determined by the plasma temperature. At a temperature of 5 eV, in good agreement with the time-average measurements of 3–4 eV, the energy loss in each capillary is predicted to be ~20% [33]. The energy transmission should improve at higher intensity, before the onset of wave breaking, due to laser-driven plasma heating mitigating inverse bremsstrahlung absorption effects. Note also that a small deviation from a circular cross-section (aspect ratio up to 1.2) is of no consequence for the laser waveguiding process.

5. Summary

Femtosecond laser micromachining is an effective technique for producing CDWs and appropriate acceleration of the scanning laser enables formation of a linear taper in the capillary cross-section. A strong taper of mean diameter 305 μm to 183 μm over a length of 40 mm shows that the range of diameters used in LWFA and CPRA applications can be met by this technique. Experimental data show that the CDWs guide low intensity laser pulses efficiently with no reduction in energy transmission in the tapered capillaries. Micromachining controllability means that the final waveguide parameters can be tailor-made to suit particular application requirements and this may extend to nonlinear capillary structures for further enhancement of accelerator or amplifier behaviour.

Acknowledgments

We acknowledge the support of the U.K. EPSRC, the EC's Seventh Framework Programme (LASERLAB-EUROPE/LAPTECH, grant agreement no. 228334) and the Extreme Light Infrastructure (ELI) European Project. We thank T. McCanny and D. Clark for technical support.

Appendix A. Single laser scan line ablation

For a laser pulse with a Gaussian intensity profile given by $I(r) = I_0 \exp(-ar^2)$ where I_0 is the peak intensity, $a = 4ln(2)/w_0^2$ and w_0 is the full-width at half-maximum, the cross-section of a single scan line is also Gaussian, as shown in Fig. A1 [34]. Defining the volume of material removed by a single femtosecond laser pulse as V_{pulse}, the generated depth profile for a single laser pulse is given by

$$P_{\text{pulse}}(\vec{r}) = V_{\text{pulse}} \frac{a}{\pi} e^{-a|\vec{r}|^2}, \tag{A1}$$

and that of a scanning trajectory $\vec{r}(t)$is given by

$$P(\vec{r}_0) = \int_0^\infty P_{\text{pulse}}\left(\vec{r}(t) - \vec{r}_0\right) f \, dt, \tag{A2}$$

where f is the laser pulse repetition rate. A continuous approximation of the laser can apply when the scan velocity $v \ll w_0 f$. For constant motion in the y-direction with velocity v, defined by $\vec{r}(t) = vt\hat{e}_y$ and $\vec{r}_0 = x_0\hat{e}_x + y_0\hat{e}_y$, the profile becomes

$$P_{\text{scanline}}(x_0, y_0) = \int_{-\infty}^{\infty} V_{\text{pulse}} f \frac{a}{\pi} e^{-a\left[(vt-y_0)^2 + x_0^2\right]} dt, \tag{A3}$$

$$= V_{\text{pulse}} f \frac{1}{|v|} \frac{\sqrt{a}}{\sqrt{\pi}} e^{-ax_0^2}. \tag{A4}$$

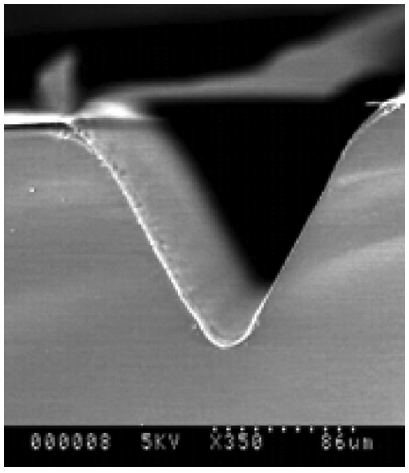

Figure A1. Electron microscope image showing the machined profile produced by a single femtosecond laser scan line.

https://doi.org/10.1017/S0022377812000062 Published online by Cambridge University Press

The removed area of a cross-section of one single scan line is, therefore, given by

$$A_{\text{scanline}} = V_{\text{pulse}} f \frac{1}{|v|}. \tag{A5}$$

Appendix B. Linearly tapered trajectories

The profile of a linearly tapered channel is described by $r(x) = r_1 + \alpha x$ and the number of scan lines N is constant over its length. From (A5), $A_{\text{scanline}} \propto 1/|v|soA_{\text{total}}(x)v(x) \sim r(x)^2 v(x)$ is constant, that is

$$r_1^2 v(0) = r(x)^2 v(x). \tag{B1}$$

The ratio between the start and end velocities is simply the square of the ratio of the radii given by

$$\frac{v(L)}{v(0)} = \left(\frac{r_1}{r_2}\right)^2. \tag{B2}$$

In general, this results in $v(x)$ being defined as

$$v(x) = \frac{r_1^2 v(0)}{(r_1 + \alpha x)^2}, \tag{B3}$$

and with separation of variables $x(t)$ can be found for $\alpha \neq 0$, thus

$$\int_0^x (r_1 + \alpha x)^2 dx = \int_0^t r_1^2 v(0)\, dt, \tag{B4}$$

$$x(t) = \frac{1}{\alpha}\left(\sqrt[3]{-3x_0 r_1^2 v(0)\alpha + 3t r_1^2 v(0)\alpha + r_1^3} - r_1\right). \tag{B5}$$

For $x_0 = 0$, this results in the tapered channel trajectory (1)–(3).

References

[1] Esarey, E., Sprangle, P., Krall, J. and Ting, A. 1997 *IEEE J. Quantum Electron.* **33**, 1879.

[2] Tajima, T. and Dawson, J. M. 1979 *Phys. Rev. Lett.* **43**, 267.

[3] Joshi, C. 2007 *Phys. Plasmas* **14**, 055501.

[4] Leemans, W. P., Nagler, B, Gonsalves, A. J., Toth, C., Nakamura, K., Geddes, C. G. R., Esarey, E., Schroeder C. B. and Hooker S. M. 2006 *Nature Phys.* **2**, 696.

[5] Cipiccia, S., Islam, M. R., Ersfeld, B., Shanks, R. P., Brunetti, E., Vieux, G., Yang, X., Issac, R. C., Wiggins, S. M., Welsh, G. H., Anania, M. P., Maneuski, D., Montgomery, R., Smith, G., Hoek, M., Hamilton, D. J., Lemos, N. R. C., Symes, D., Rajeev, P. P., O'Shea, V., Dias, J. M. and Jaroszynski, D. A. 2011 *Nature Phys.* **7**, 867.

[6] Malkin, V. M., Shvets, G. and Fisch, N. J. 2000 *Phys. Rev. Lett.* **84**, 1208.

[7] Ersfeld, B. and Jaroszynski, D. A. 2005 *Phys. Rev. Lett.* **95**, 165002.

[8] Vieux, G., Lyachev, A., Yang, X., Ersfeld, B., Farmer, J. P., Brunetti, E., Issac, R. C., Raj, G., Welsh, G. H., Wiggins, S. M. and Jaroszynski, D. A. 2011 *New J. Phys.* **13**, 063042.

[9] Malka, V., Faure, J., Gauduel, Y. A., Lefebvre, E., Rousse, A. and Phuoc, K. T. 2008 *Nature Phys.* **4**, 447.

[10] Schroeder, C. B., Esarey, E., Geddes, C. G. R., Benedetti, C. and Leemans, W. P. 2010 *Phys. Rev. ST Accel. Beams* **13**, 101301.

[11] Strickland, D. and Mourou, G. 1985 *Opt. Commun.* **56**, 219.

[12] Ross, I. N., Matousek, P., Towrie, M., Langley, A. J. and Collier, J. L. 1997 *Opt. Commun.* **144**, 125.

[13] Mourou, G. A., Tajima, T. and Bulanov, S. V. 2006 *Rev. Mod. Phys.* **78**, 309.

[14] Spence, D. J. and Hooker, S. M. 2001 *Phys. Rev.* E **63**, 015401.

[15] Gattass, R. R. and Mazur, E. 2008 *Nature Photonics* **2**, 219.

[16] Jaroszynski, D. A., Bingham, R., Brunetti, E., Ersfeld, B., Gallacher, J., van der Geer, B., Issac, R., Jamison, S. P., Jones, D., de Loos, M., Lyachev, A., Pavlov, V., Reitsma, A., Saveliev, Y., Vieux G. and Wiggins, S. M. 2006 *Phil. Trans. R. Soc.* A **364**, 689.

[17] Stuart, B. C., Feit, M. D., Herman, S., Rubenchik, A. M., Shore, B. W. and Perry, M. D. 1996 *Phys. Rev.* B **53**, 1749.

[18] Kaganovich, D., Sasorov, P., Cohen, C. and Zigler, A. 1999 *Appl. Phys. Lett.* **75**, 772.

[19] Katsouleas, T. 1986 *Phys. Rev.* A **33**, 2056.

[20] Sprangle, P., Penano, J. R., Hafizi, B., Hubbard, R. F., Ting, A., Gordon, D. F., Zigler, A. and Antonsen, Jr., T. M. 2002 *Phys. Plasmas* **9**, 2364.

[21] Rittershofer, W., Schroeder, C. B., Esarey, E., Grüner, F. J. and Leemans, W. P. 2010 *Phys. Plasmas* **17**, 063104.

[22] Abuazoum, S., Wiggins, S. M., Issac, R. C., Welsh, G. H., Vieux, G., Ganciu, M. and Jaroszynski, D. A. 2011 *Rev. Sci. Instrum.* **82**, 063505.

[23] Jaroszynski, D. A., Ersfeld, B., Giraud, G., Jamison, S., Jones, D. R., Issac, R. C., McNeil, B. W. J., Phelps, A. D. R., Robb, G. R. M., Sandison, H., Vieux, G., Wiggins, S. M. and Wynne, K. 2000 *Nucl. Instrum. Methods Phys. Res.,* Sec. A **445**, 317.

[24] Travis, J and Kring, J. 2006 Labview for Everyone: Graphical Programming Made Easy and Fun, 3rd edition, Prentice Hall; National Instruments. http://www.ni.com/labview/.

[25] Ashkenazy, J., Kipper, R. and Caner, M. 1991 *Phys. Rev.* A **43**, 5568.

[26] Brobova, N. A., Esaulov, A. A., Sakai, J.-I., Sasorov, P. V., Spence, D. J., Butler, A., Hooker, S. M. and Bulanov, S. V. 2001 *Phys. Rev.* E **65**, 016407.

[27] Gonsalves, A. J., Rowlands-Rees, T. P., Broks, B. H. P., van der Mullen, J. J. A. M. and Hooker, S. M. 2007 *Phys. Rev. Lett.* **98**, 025002.

[28] Jang, D. G., Kim, M. S., Nam, I. H., Uhm, H. S. and Suk, H. 2011 *Appl. Phys. Lett.* **99**, 141502.

[29] Broks, B. H. P., Garloff, K. and van der Mullen, J. J. A. M. 2005 *Phys. Rev.* E **71**, 016401.

[30] Torres, J., Palomares, J. M., Sola, A., van der Mullen, J. J. M. and Gamero, A. 2007 *J. Phys. D.: Appl. Phys.* **40**, 5929.

[31] Abuazoum, S., Wiggins, S. M., Ersfeld, B., Hart, K., Vieux, G., Yang, X., Welsh, G. H., Issac, R. C., Reijnders, M. P., Jones, D. R. and Jaroszynski, D. A. 2012 *Appl. Phys. Lett.* **100**, 014106.

[32] Hughes, T. P. 1975 *Plasmas and Laser Light*. Adam Hilger.

[33] Hora, H. and Wilhelm, H. 1970 *Nucl. Fusion* **10**, 111.

[34] Borowiec, A., Mackenzie, M., Weatherly, G. C. and Haugen, H. K. 2003 *Appl. Phys.* A **76**, 201.

https://doi.org/10.1017/S0022377812000062 Published online by Cambridge University Press